Journal of Computational Physics 228 (2009) 5888–5907

Contents lists available at ScienceDirect

Journal of Computational Physics

journal homepage: www.elsevier.com/locate/jcp

An adaptive SPH method for strong shocks

Leonardo Di G. Sigalotti [a,*], Hender López [b], Leonardo Trujillo [a,1]

[a] Centro de Fisica, Instituto Venezolano de Investigaciones Científicas, IVIC, Apartado Postal 20632, Caracas 1020-1, Venezuela
[b] Departament d'Enginyeria Electrònica, Universitat Autònoma de Barcelona, 08193 Bellaterra, Barcelona, Spain

ARTICLE INFO

Article history:
Received 18 November 2008
Received in revised form 19 April 2009
Accepted 28 April 2009
Available online 9 May 2009

Keywords:
Lagrangian: Particle method
Numerical methods
Ideal compressible flows
SPH: Godunov's method

ABSTRACT

We propose an alternative SPH scheme to usual SPH Godunov-type methods for simulating supersonic compressible flows with sharp discontinuities. The method relies on an *adaptive density kernel estimation* (ADKE) algorithm, which allows the width of the kernel interpolant to vary locally in space and time so that the minimum necessary smoothing is applied in regions of low density. We have performed a von Neumann stability analysis of the SPH equations for an ideal gas and derived the corresponding dispersion relation in terms of the local width of the kernel. Solution of the dispersion relation in the short wavelength limit shows that stability is achieved for a wide range of the ADKE parameters. Application of the method to high Mach number shocks confirms the predictions of the linear analysis. Examples of the resolving power of the method are given for a set of difficult problems, involving the collision of two strong shocks, the strong shock-tube test, and the interaction of two blast waves.

1. Introduction

Since its invention [1,2], the method of Smoothed Particle Hydrodynamics (SPH) has been applied to a large number of complex, nonlinear phenomena, ranging from large-scale cosmological and astrophysical flows [3–12] to small-scale fluids (liquids and gases) [13–21] and solids [22–27]. SPH is a fully Lagrangian method based on kernel interpolation in which matter is discretized into point particles which move with the flow without exchanging mass. The parameter indicating the resolution in a continuum description of the flow with a certain interpolating kernel function is referred to as the smoothing length h. As the particles move with the fluid flow, an inhomogeneous particle distribution will be produced. In standard SPH the smoothing length is adjusted to the particle distribution by allowing each particle to have a unique value of h that varies with time and space so that the number of neighboring particles within the interpolation space is kept roughly constant. However, it has been recently shown that the fidelity of SPH simulations greatly improves when the number of neighbors is kept exactly constant because this condition results in an effective reduction in the rates of numerical dissipation and diffusion [28]. Although the method is well suited to hydrodynamic problems that have large empty regions and moving boundaries, it gives a rather poor description of strong shock phenomena. In general, conventional SPH yields shock profiles that are not as sharp as those for exact, or approximated, Riemann solutions.

Reformulations of SPH for handling strong shocks and discontinuities with the same accuracy of high quality Godunov-type schemes have been independently proposed by Monaghan [29], Inutsuka [30], Cha and Whitworth [31], and Ferrari et al. [32]. A common feature of all these methods is the combination of standard SPH with Riemann solvers. In particular, Monaghan [29] focused on relating the dissipative terms in the SPH equations to those appearing in Riemann formulations

* Corresponding author. Tel.: +58 212 5041369; fax: +58 212 5041148.
E-mail addresses: leonardo.sigalotti@gmail.com (L.D.G. Sigalotti), hender.lopez@gmail.com (H. López), trujillo@lpm.u-nancy.fr (L. Trujillo).
[1] Also at: The Abdus Salam International Centre for Theoretical Physics, ICTP, Strada Costiera 11, 34014 Trieste, Italy.

0021-9991/$ - see front matter © 2009 Elsevier Inc. All rights reserved.
doi:10.1016/j.jcp.2009.04.041

and working with the total energy equation rather than the thermal energy equation. Inutsuka [30] and Cha and Whitworth [31] proposed similar schemes where the force acting on each particle is determined by solving the Riemann problem in the vicinity of the midpoint between each pair of interacting particles. This procedure is the analog to that employed in Godunov-type methods which use a Riemann solver to calculate the flux at the border of each computational cell. More recently, Ferrari et al. [32] devised an SPH method that relies on the use of Godunov-type schemes in Lagrangian coordinates. As expected, SPH formulations based on Riemann solvers have performed well at solving sharp discontinuities for a variety of shock problems.

Alternative SPH formulations for handling strong shocks, which do not rely on Riemann solvers, have also started to appear. A method that yields accurate solutions for the problem of two interacting blast waves [33] and for a variety of difficult magnetohydrodynamic shock problems was developed by Børve et al. [34]. In their approach, the particle distribution is used to shape the smoothing length profile and not *vice versa* which has normally been the case. The particle distribution is then redefined at appropriate intervals in accordance with a previous update of h. This makes the particle distribution more regular than with ordinary SPH, thereby reducing the errors associated with the estimation of gradients. Moreover, an SPH method based on an *adaptive density kernel estimation* (ADKE) in the way described by Silverman [35] was recently reported by Sigalotti et al. [36]. When it is applied to supersonic compressible flows with sharp discontinuities, as in the classical Sod's [37] shock-tube problem and its variants, the accuracy of the results becomes comparable, and in most cases superior, to that obtained with Godunov-type methods and SPH formulations based on Riemann solutions. Unlike existing adaptive SPH schemes, this class of estimates requires a less broad kernel in zones where the density is low, implying that the minimum necessary smoothing is applied in these regions. This feature allows for a unique scheme that handles strong shocks and rarefactions the same way and improves the accuracy and stability near sharp discontinuities.

The ADKE algorithm combines intrinsic features of both the kernel and nearest neighbor approaches such that the amount of smoothing applied to the data is minimized. The heart of the method lies on estimating the density at the location of particles to construct a collection of *bandwidth factors*, or kernels, in order to allow the final smoothing length to vary from point to point. The definition of the local bandwidth factors involves two free parameters, which can be conveniently chosen to reduce the rates of numerical dissipation and diffusion. Through a linear analysis of the SPH equations, we derive the corresponding dispersion relation and solve it in the short wavelength limit to obtain the dependence of the frequency on the local bandwidth factor. The solution of the dispersion relation indicates, in a first approximation, that stability can be guaranteed for a wide range of the ADKE parameters. While this analysis validates the results obtained by Sigalotti et al. [36] for a suite of well-known one- and two-dimensional shock problems, in this paper we show that the scheme is also able to accurately reproduce the solution of more difficult tests, involving the collision of two strong shocks [38], the shock-tube problem of Fryxell et al. [39] containing a very strong shock, and the interaction of two blast waves introduced by Woodward and Colella [33].

2. The Euler equations

The equations that govern the dynamics of a compressible fluid, for which the effects of body forces, viscous stresses, and heat flux are neglected, written in Lagrangian coordinates (x,t) in one-dimensional space, are

$$\frac{D\rho}{Dt} = -\rho\frac{\partial v}{\partial x}, \tag{1}$$

$$\rho\frac{Dv}{Dt} = -\frac{\partial p}{\partial x}, \tag{2}$$

$$\rho\frac{DU}{Dt} = -p\frac{\partial v}{\partial x}, \tag{3}$$

where $D/Dt = \partial/\partial t + v\partial/\partial x$ is the substantial or material time derivative, ρ is the density, v is the velocity, U is the specific internal energy, and p is the pressure defined by the equation of state of an ideal gas

$$p = (\gamma - 1)\rho U, \tag{4}$$

where γ is the ratio of specific heats.

3. The SPH equations

In standard SPH, the density ρ_i of particle i is calculated using the summation interpolant

$$\rho_i = \sum_{j=1}^{N} m_j W_{ij}, \tag{5}$$

where the summation includes the contribution of particle i itself and $W_{ij} = W(|x_i - x_j|, h)$ is the kernel, or weight, function and h is the smoothing length. In practice, smoothing kernels with compact supports are almost always used, so that a finite

number $\mathcal{N}_s$ of particles around x_i contribute to the estimate of ρ_i. When Eq. (5) is used to calculate the density, variational consistency will demand using symmetrized SPH representations for Eqs. (2) and (3) [40].

The symmetrized SPH discretization of the Euler and specific internal energy equations are

$$\frac{dv_i}{dt} = -\sum_{j=1}^{N} m_j \left(\frac{p_i}{\rho_i^2} + \frac{p_j}{\rho_j^2} + \Pi_{ij} \right) \frac{\partial W_{ij}}{\partial x_i}, \tag{6}$$

$$\frac{dU_i}{dt} = -\frac{1}{2}\sum_{j=1}^{N} m_j \left[\left(\frac{p_i}{\rho_i^2} + \frac{p_j}{\rho_j^2} + \Pi_{ij} \right)(v_j - v_i) + 2H_{ij}(x_j - x_i) \right] \frac{\partial W_{ij}}{\partial x_i}. \tag{7}$$

The derivation of these symmetrizations are explained in [36]. In calculations of compressible flows involving the formation and propagation of shocks, an artificial viscosity term, Π_{ij}, must be added to the SPH equations to dissipate postshock oscillations in the solution and avoid particle interpenetration in high Mach number collisions. As in [36], for the artificial viscosity we use the standard formulation [41–43]

$$\Pi_{ij} = \frac{-\alpha \bar{c}_{ij}\mu_{ij} + \beta \mu_{ij}^2}{\bar{\rho}_{ij}}, \tag{8}$$

if $(v_i - v_j)(x_i - x_j) < 0$ and zero otherwise. Here

$$\mu_{ij} = \frac{(v_i - v_j)(x_i - x_j)}{h_{ij}(x_{ij}^2/h_{ij}^2 + \eta^2)}, \tag{9}$$

where $\bar{c}_{ij}$, $\bar{\rho}_{ij}$, and h_{ij} are the average sound speed, density, and smoothing length between particles i and j, respectively, and $x_{ij} = x_i - x_j$. For the calculations of this paper we take $\alpha = \beta = 1$ and $\eta^2 = 0.01$. With this choice of η^2 smoothing of the velocity will only take place when the particle spacing is less than $0.1\,h$. The linear term in Eq. (8) produces a shear and bulk viscosity, whereas the quadratic term is introduced to handle high Mach number shocks. This form of the artificial viscosity conserves linear momentum and guarantees a positive definite entropy change due to dissipation. The use of an artificial viscosity in Lagrangian methods may induce errors in the form of excessive heating. These errors, which are commonly referred to as wall-heating errors after Noh [44], often occur in calculations of infinite strength shocks. In order to significantly reduce these errors, we add an artificial heat conduction term, H_{ij}, to the specific internal energy given by [36]

$$H_{ij} = \frac{2\mathcal{H}_{ij}(U_i - U_j)}{\bar{\rho}_{ij}h_{ij}^2\left(x_{ij}^2/h_{ij}^2 + \eta^2\right)}, \tag{10}$$

where $\mathcal{H}_{ij}$ is the averaged artificial conduction coefficient (normalized to the density) between particles i and j, with $\mathcal{H}_i$ defined as

$$\mathcal{H}_i = g_1 h_i c_i + g_2 h_i^2 \left[\left| \frac{\partial v_i}{\partial x_i} \right| - \frac{\partial v_i}{\partial x_i} \right], \tag{11}$$

where g_1 and g_2 are constants of the order of unity. The artificial heat flux is activated only when the artificial viscosity is nonzero. The first term on the right-hand side of Eq. (11) is linear in h and is a function of the local sound speed, whereas the second term, which is quadratic in h, takes a finite positive value only when there is a compression ($\nabla \cdot \mathbf{v} < 0$) and vanishes otherwise. In the vicinity of a sharp discontinuity, this term dominates over the linear one and sets the magnitude of the conduction coefficient. In addition, the SPH (Eqs. (5)–(7)) must be solved simultaneously with the equation

$$\frac{Dx_i}{Dt} = v_i, \tag{12}$$

for the evolution of the particle positions.

The scheme implemented here differs from other formulations of the method in one important concern: the smoothing is based on an ADKE procedure similar to the one proposed by Silverman [35]. Here we will only describe the most relevant aspects of the method and refer the reader to [36,45] for a complete description. Most existing adaptive SPH calculations are based on the nearest neighbor approach [46], in which broader kernels are used in regions of lower density. In contrast, the ADKE method copes with this problem by choosing the kernel such that the amount of smoothing that is applied to the data is minimized in regions of low density. In the first place, the method consists of calculating an initial, or *pilot*, density estimate from the particle distribution using the summation interpolant

$$\tilde{\rho}_i = \sum_{j=1}^{N} m_j W(x_{ij}, h_0), \tag{13}$$

where h_0 is chosen by reference to an initial distribution. In practice, $h_0 = D\Delta x_0$, where D is some dilation factor of the initial uniform interparticle separation Δx_0. In the second step, local bandwidth factors, λ_i, are constructed for each particle i from the pilot density estimates according to

$$\lambda_i = \kappa\left(\frac{\tilde{\rho}_i}{\bar{g}}\right)^{-\epsilon}, \tag{14}$$

where $\bar{g}$ is a geometric mean of the pilot density, i.e.

$$\log \bar{g} = \frac{1}{N}\sum_{j=1}^{N} \log \tilde{\rho}_j, \tag{15}$$

κ is a constant scaling factor of the order of unity, and ϵ is the sensitivity parameter defined in the interval $0 \leqslant \epsilon \leqslant 1$. In the third step, the adaptive estimator is obtained by redefining the width of the kernel at the location of particle i as $h_i = \lambda_i h_0$ and by recalculating the density using Eq. (13) with h_0 replaced by h_i. In order to ensure conservation of linear momentum and total energy the actual kernel estimate that is employed in Eqs. (5)–(7) to update the density, velocity, and specific internal energy of the particles is based on the symmetrized form [46]

$$W_{ij} = \frac{1}{2}\left[W(x_{ij}, h_i) + W(x_{ij}, h_j)\right]. \tag{16}$$

If we set $\epsilon = 0$ in Eq. (14), the method reduces to the fixed width kernel approach, while for $\epsilon = 1$ the local bandwidth factors will attain the largest sensitivity to variations in the density distribution, implying a greater difference between the smoothing lengths in different parts of the sample.

4. The SPH dispersion relation

If we assume a traveling plane wave of the form

$$\phi = \phi_0 + \Phi e^{i(kx_0 - \omega t)}, \tag{17}$$

where ϕ may be either x, ρ, v, p, or U, k is the wavenumber, ω is the angular frequency, and Φ is a complex amplitude, and define the unperturbed state (ϕ_0) as a homogeneous isotropic fluid at rest (i.e., $v_0 = 0$), linearization of Eqs. (1)–(4) leads to the well-known dispersion relation for the propagation of longitudinal acoustic waves in a fluid at rest

$$\omega = \pm c_0 k, \tag{18}$$

where $c_0^2 = \gamma(\gamma - 1)U_0$ is the adiabatic sound speed.

When standard SPH is applied to the simulation of deforming elastic solids, it becomes unstable to negative stress. This instability, which is most commonly known as the tensile instability, causes an unphysical clumping of the SPH particles towards stable configurations. The origin of the instability was first studied by Swegle et al. [47] through an analysis of the SPH dispersion relation for elastic waves. Using similar linear analyses, Monaghan [26] and Gray et al. [27] found that the tensile instability can be prevented by adding an artificial stress to the governing SPH equations. The instability is also known to occur in gas dynamics where the pressure is always positive [48]. In a comprehensive study, Morris [49,50] investigated the nature of this and other instabilities in depth, finding that the stability of SPH in general improves when higher-order interpolants are used as kernels. The tensile instability was also found to arise in magnetohydrodynamic (MHD) problems from a change in sign of the magnetic field stress tensor [4]. A remedy to this instability was first proposed by Morris [50], and more recently, by Børve et al. [51] through an analysis of the dispersion relation for MHD waves. Similar linear perturbation analyses were also recently developed by Cha and Whitworth [31] and Sigalotti and López [45] for gas dynamic problems in the context of SPH Godunov-type and SPH-ADKE methods, respectively. In the present study, the von Neumann stability analysis of the SPH equations differs from most previous analyses in that the resulting dispersion relation is derived in terms of the local bandwidth factor, λ_i, defined by Eq. (14), in order to validate the ADKE algorithm for strong shock problems.

4.1. SPH with artificial viscosity and with artificial heating

We first derive the SPH dispersion relation for the general case in which both the artificial viscosity and the artificial conductive heating are retained in Eqs. (6) and (7). For simplicity, we consider an initial system where all particles are aligned along the x-axis and equally spaced with separation Δx_0. Therefore, all particles have the same mass $m = \rho_0 \Delta x_0$. As for the continuum case, a small perturbation is added to the system such that

$$\begin{pmatrix} x_i \\ \rho_i \\ v_i \\ p_i \\ U_i \end{pmatrix} = \begin{pmatrix} x_{0,i} \\ \rho_0 \\ 0 \\ p_0 \\ U_0 \end{pmatrix} + \begin{pmatrix} X \\ \mathcal{D} \\ V \\ (\gamma - 1)[\rho_0 \mathcal{U} + U_0 \mathcal{D}] \\ \mathcal{U} \end{pmatrix} e^{i(kx_{0,i} - \omega t)}. \tag{19}$$

With the aid of the following definitions:

$$A_i = \Delta x_0 \sum_{j=1}^{N} \sin(kx_{0,ij}) \frac{\partial W_{ij}}{\partial x_{0,i}}, \tag{20}$$

$$B_i = \Delta x_0 \sum_{j=1}^{N} [1 - \cos(kx_{0,ij})] \frac{\partial^2 W_{ij}}{\partial x_{0,i}^2}, \tag{21}$$

$$C_i = \Delta x_0 \sum_{j=1}^{N} \frac{1}{x_{0,ij}} \sin(kx_{0,ij}) \frac{\partial W_{ij}}{\partial x_{0,i}}, \tag{22}$$

$$D_i = \Delta x_0 \sum_{j=1}^{N} \sin(kx_{0,ij}) \frac{\partial^2 W_{ij}}{\partial x_{0,i}^2}, \tag{23}$$

$$E_i = \Delta x_0 \sum_{j=1}^{N} [1 + \cos(kx_{0,ij})] \frac{\partial W_{ij}}{\partial x_{0,i}}, \tag{24}$$

$$F_i = \Delta x_0 \sum_{j=1}^{N} \frac{1}{x_{0,ij}} [1 - \cos(kx_{0,ij})] \frac{\partial W_{ij}}{\partial x_{0,i}}, \tag{25}$$

$$G_i = \Delta x_0 \sum_{j=1}^{N} [1 - \cos(kx_{0,ij})] \frac{\partial W_{ij}}{\partial x_{0,i}}, \tag{26}$$

where $x_{0,ij} = x_{0,i} - x_{0,j}$, substitution of relations (19) into Eqs. (5) and (12) yields the linearized equations

$$\omega \mathcal{D} = -\rho_0 V A_i, \tag{27}$$

$$\omega X = iV, \tag{28}$$

while the momentum Eq. (6) and the specific internal energy Eq. (7) become

$$\omega^2 + \left[\alpha h_i c_0 (C_i - iF_i) + (\gamma - 1)(A_i + iE_i)\frac{\mathcal{U}}{V}\right]\omega + \frac{p_0}{\rho_0}\{A_i^2 - 2B_i + E_i G_i - i[A_i(G_i - E_i) + 2D_i]\} = 0, \tag{29}$$

and

$$[\omega + 2g_1 h_i c_0 (C_i - iF_i)]\frac{\mathcal{U}}{V} = -\frac{p_0}{\rho_0}(A_i - iG_i), \tag{30}$$

respectively, where we have made use of Eqs. (27) and (28). Introducing the dimensionless frequency

$$\Omega = \frac{\gamma^{1/2}\Delta x_0 \omega}{c_0}, \tag{31}$$

and combining Eqs. (29) and (30), we obtain the dispersion relation

$$\Omega^4 + \tilde{a}\Omega^3 + \tilde{b}\Omega^2 + \tilde{c}\Omega + \tilde{d} = 0, \tag{32}$$

where

$$\frac{\tilde{a}}{\Delta x_0} = \gamma^{1/2} h_i [(4g_1 + \alpha)C_i - i\alpha F_i], \tag{33}$$

$$\frac{\tilde{b}}{\Delta x_0^2} = 4g_1 h_i^2 \gamma [(\alpha + g_1)C_i^2 + g_1 F_i^2] - (\gamma - 2)(A_i^2 + E_i G_i) - 2B_i - i[4\alpha g_1 h_i^2 \gamma C_i F_i + (\gamma - 2)A_i(E_i - G_i) + 2D_i], \tag{34}$$

$$\begin{aligned}\frac{\tilde{c}}{\Delta x_0^3} = {} & 2g_1 h_i \gamma^{1/2}\left\{2\alpha g_1 h_i^2 \gamma C_i (C_i^2 + F_i^2) + (\gamma - 1)A_i F_i (E_i - G_i) - C_i[(\gamma - 3)(A_i^2 + E_i G_i) + 4B_i]\right\} \\ & - i2g_1 h_i \gamma^{1/2}\left\{2\alpha g_1 h_i^2 \gamma F_i (C_i^2 + F_i^2) + (\gamma - 1)F_i (A_i^2 + E_i G_i) + C_i[(\gamma - 3)A_i (E_i - G_i) + 4D_i]\right\},\end{aligned} \tag{35}$$

$$\frac{\tilde{d}}{\Delta x_0^4} = 4g_1^2 h_i^2 \gamma (C_i^2 + F_i^2)\left\{A_i^2 + E_i G_i + i[A_i(E_i - G_i) - 2D_i]\right\}. \tag{36}$$

Eq. (32) is a quartic complex polynomial relating the frequency to the wavenumber. Its solution admits four complex roots. The response to small perturbations will be unstable if the imaginary part of at least one of these complex roots is positive, that is, if $\mathrm{Im}(\Omega) > 0$. In this case, the perturbations, once having arisen, will grow indefinitely with time. In contrast, the response will be stable either if the perturbations decay exponentially with time, in which case $\mathrm{Im}(\Omega) < 0$, or remain constant in amplitude, in which case $\mathrm{Im}(\Omega) = 0$. The expressions for the above coefficients simplify if we realize that $A_i = C_i = D_i = 0$ for a string of perfectly equidistant particles.

4.2. SPH without artificial viscosity and without artificial heating

If we set $\Pi_{ij} = H_{ij} = 0$ in Eqs. (6) and (7), the corresponding dispersion relation can be obtained from Eq. (32) by setting $\alpha = g_1 = 0$. In this case, all the coefficients vanish identically with the exception of $\tilde{b}$ and Eq. (32) takes the form

$$\frac{\Omega^2}{\Delta x_0^2} = (\gamma - 2)(A_i^2 + E_i G_i) + 2B_i + i[(\gamma - 2)A_i(E_i - G_i) + 2D_i], \tag{37}$$

which can be solved straightforwardly for Ω. In the limit when $k \ll 1$ and $h \gg \Delta x_0$, the summations in Eqs. (20)–(26) can be approximated by integrals. Therefore, if we define the Fourier transform of the kernel W as

$$\widetilde{W}(k) = \frac{1}{\sqrt{2\pi}} \int_{-\infty}^{+\infty} W(x)\cos(kx)dx + i\frac{1}{\sqrt{2\pi}} \int_{-\infty}^{+\infty} W(x)\sin(kx)dx = \widetilde{W}_c + i\widetilde{W}_s, \tag{38}$$

it is a trivial task to show that $A_i \to -k\widetilde{W}_c$, $B_i \to k^2\widetilde{W}_c$, $D_i \to -k^2\widetilde{W}_s$, $E_i \to k\widetilde{W}_s$, and $G_i \to -k\widetilde{W}_s$. Replacing these forms into Eq. (37) and taking the limit of long wavelengths, $k \to 0$, we find that $\widetilde{W}_c \to 1$ and $\widetilde{W}_s \to 0$, and therefore Eq. (37) reduces exactly to the continuum dispersion relation (18).

Since $A_i = D_i = 0$ for a linear array of equally spaced particles, the imaginary part of Eq. (37) vanishes and Ω^2 becomes real, yielding the simplified expression for the dimensionless frequency in the absence of dissipation

$$\frac{\Omega_{00}^2}{\Delta x_0^2} = (\gamma - 2)E_i G_i + 2B_i, \tag{39}$$

which can be also shown to reduce to Eq. (18) for long wavelengths.

4.3. SPH with artificial viscosity and without artificial heating

We now consider the case when $g_1 = 0$, i.e., when the artificial heat flux is dropped from Eq. (7) and only the artificial viscosity term is retained. In this case, the dispersion relation reduces to the quadratic complex polynomial

$$\Omega^2 + \tilde{a}\Omega + \tilde{b} = 0, \tag{40}$$

with

$$\frac{\tilde{a}}{\Delta x_0} = \alpha h_i \gamma^{1/2}(C_i - iF_i), \tag{41}$$

$$\frac{\tilde{b}}{\Delta x_0^2} = -(\gamma - 2)(A_i^2 + E_i G_i) - 2B_i - i[(\gamma - 2)A_i(E_i - G_i) + 2D_i]. \tag{42}$$

For a linear array of uniformly spaced particles ($A_i = C_i = D_i = 0$), the solution to Eq. (40) can be written as

$$\Omega_{\mathrm{AV},0} = \pm\frac{1}{2}[-\alpha^2 h_i^2 \gamma(\Delta x_0 F_i)^2 + 4\Omega_{00}^2]^{1/2} + i\frac{1}{2}\alpha h_i \gamma^{1/2}\Delta x_0 F_i. \tag{43}$$

If the radicand is negative, $\Omega_{\mathrm{AV},0}$ will be a pure imaginary number. If, on the other hand, the radicand vanishes both imaginary roots will be identical.

5. Stability analysis

We discuss the stability properties of our adaptive SPH method in response to longitudinal acoustic waves propagating along the x-axis, with $k = \pi/\Delta x_0$, in the limit of short wavelengths. The rate of growth of the instability depends on the initial distribution of particles, the kernel function, the value of h, and the equation of state. For the purposes of the present analysis we shall consider an Eulerian kernel with nodal integration for various sizes of h. In the ADKE procedure, the actual width of the kernel at the position of particle i is $h_i = \lambda_i h_0$. We may therefore solve the SPH dispersion relations (32), (37) and (40) to get the dependence of the frequency on λ_i and look for the sign of the imaginary part of ω. To do so we set $h_0 = D\Delta x_0$ and consider values of $D \leqslant 4$ so that only nearest and next nearest neighbors will contribute to the sums in relations (20)–(26). When $D = 1$ or $3/2$, a total of $\mathcal{N}_s = 2$ neighbors contribute to the kernel summations. For higher sizes of the kernel support, the number of neighbors increases (i.e., $\mathcal{N}_s = 4$ for $D = 2$ or $5/2$, $\mathcal{N}_s = 6$ for $D = 3$ or $7/2$, and $\mathcal{N}_s = 8$ for $D = 4$). In addition,

we assume that in the unperturbed state the particles are uniformly placed along the x-axis and use a Gaussian kernel modified for compact support according to

$$W(q,h)=\frac{1}{\pi^{1/2}h}\begin{cases} e^{-q^2} & \text{if} \quad 0\leqslant q\leqslant 3 \\ 0 & \text{if} \quad q>3, \end{cases} \tag{44}$$

so that the particles are not allowed to interact at distances from the peak of the distribution greater than 3 h. To check the dependence of the results on the kernel, we have also used the cubic B-spline function [52]

$$W(q,h)=\frac{1}{h}\begin{cases} \frac{2}{3}-q^2+\frac{1}{2}q^3 & \text{if} \quad 0\leqslant q<1 \\ \frac{1}{6}(2-q)^3 & \text{if} \quad 1\leqslant q\leqslant 2 \\ 0 & \text{if} \quad q>2. \end{cases} \tag{45}$$

In the above expressions $q=|x|/h$, where for convenience we have shifted the position of particle i to $x_i=0$.

The solution to the perturbation problem has a temporal dependence given by $\exp(-i\omega t)=\exp[-i\mathrm{Re}(\omega)t]\exp[\,\mathrm{Im}(\omega)t]$. Thus the amplitude of the perturbation amplifies (instability) when $\mathrm{Im}(\omega)>0$ and damps out (stability) when $\mathrm{Im}(\omega)<0$. If $\mathrm{Im}(\omega)=0$, the perturbed field oscillates with neither amplifying nor damping. In the discussion of the stability we use relation (31) and express the results in terms of the dimensionless frequency Ω.

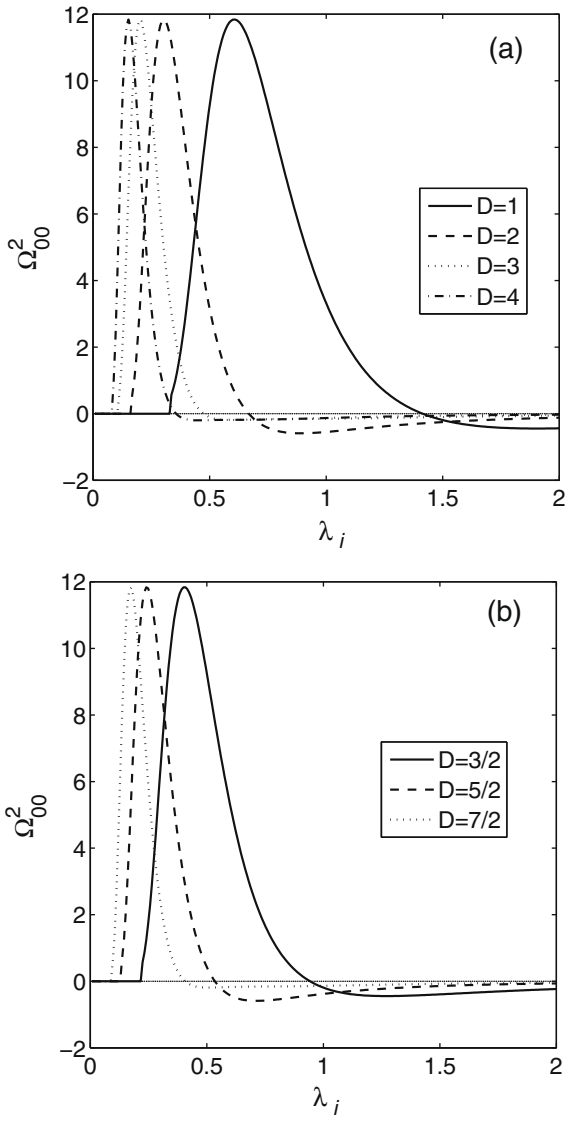

Fig. 1. Frequency as a function of the bandwidth factor, λ_i, for (a) integer and (b) fractional values of the dilation factor, D, for the case in which $\alpha=0$ (no artificial viscosity) and $g_1=0$ (no artificial conductive heat).

5.1. Case in which $\alpha = g_1 = 0$

In the absence of artificial viscosity ($\alpha = 0$) and artificial heating ($g_1 = 0$), Eq. (39) gives the dispersion relation for a linear set of equidistant particles all with the same mass. Fig. 1 shows the square of the wave frequency as a function of the bandwidth factor for varied lengths of the interpolation segment up to $D = 4$, using the Gaussian kernel (44). The curves in Fig. 1(a) depict the variation of Ω^2_{00} for integer values of D, i.e., $D = 1$ (solid line), 2 (dashed line), 3 (dotted line), and 4

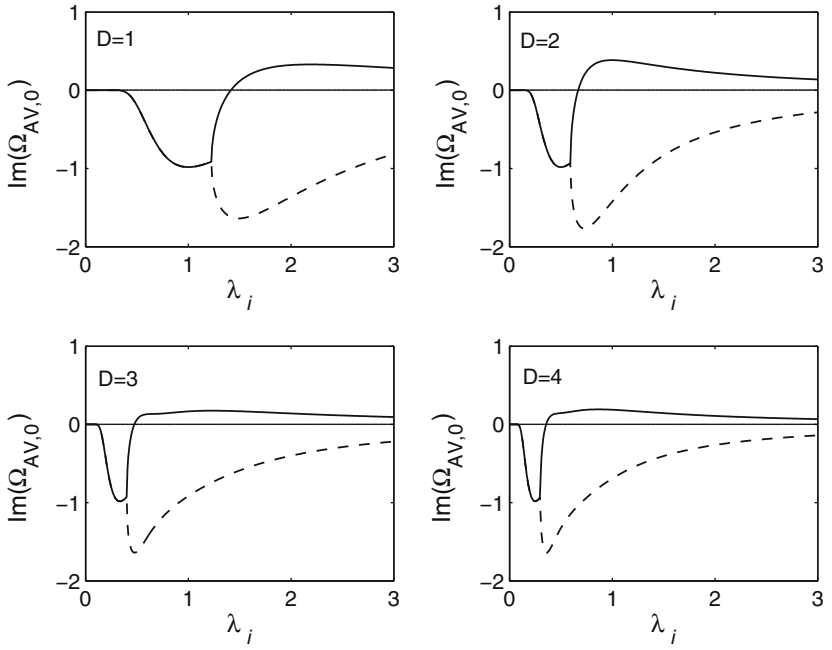

Fig. 2. Imaginary part of the frequency as a function of the bandwidth factor, λ_i, for integer values of the dilation factor, D, for the case in which $\alpha = 1$ and $g_1 = 0$. The most significant frequency corresponds to the solid line.

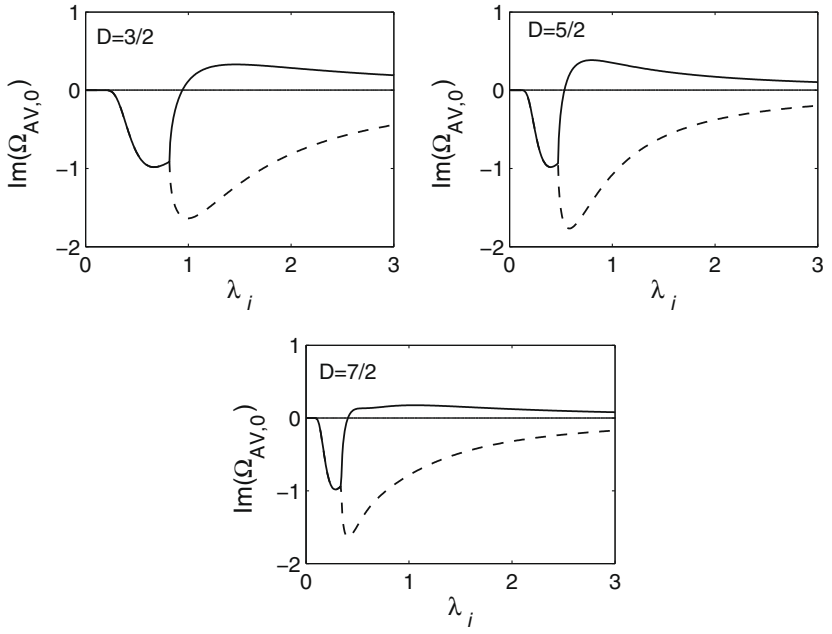

Fig. 3. Imaginary part of the frequency as a function of the bandwidth factor, λ_i, for fractional values of the dilation factor, D, for the case in which $\alpha = 1$ and $g_1 = 0$. The most significant frequency corresponds to the solid line.

(dot–dashed line), whereas those in Fig. 1(b) are for fractional values of the dilation parameter, i.e., $D = 3/2$ (solid line), $5/2$ (dashed line), and $7/2$ (dotted line). When $\Omega_{00}^2 \geqslant 0$, the two roots of Eq. (39) are real numbers. In this case, the amplitude of the perturbations will neither grow nor decrease with time. In addition, if $\Omega_{00}^2 < 0$, the frequency becomes a pure imaginary number equal to $\pm i\sqrt{\Omega_{00}}$. Since both solutions are possible, the oscillation modes may either amplify or damp, depending on whether the sign is positive or negative, respectively.

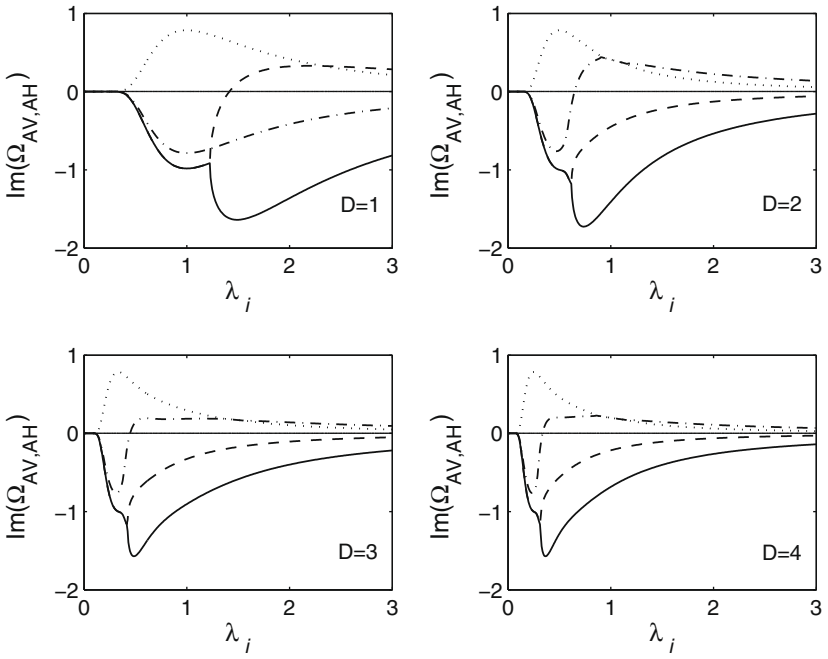

Fig. 4. Imaginary part of the frequency as a function of the bandwidth factor, λ_i, for integer values of the dilation factor, D, for the case in which $\alpha = 1$ and $g_1 = 0.2$. All four roots of Eq. (32) are shown. The most significant frequency corresponds to the dotted line.

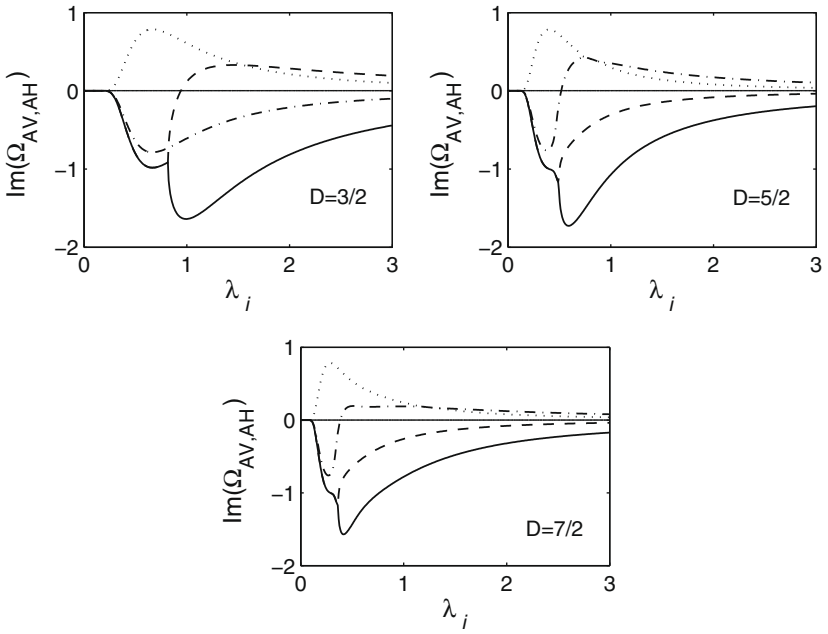

Fig. 5. Imaginary part of the frequency as a function of the bandwidth factor, λ_i, for fractional values of the dilation factor, D, for the case in which $\alpha = 1$ and $g_1 = 0.2$. All four roots of Eq. (32) are shown. The most significant frequency corresponds to the dotted line.

In particular, for $D = 1, \Omega_{00}^2 \geqslant 0$ for $\lambda_i \lesssim 1.416$ and negative for all other values larger than this. Therefore, marginal stability occurs for most frequencies. For larger values of D, the point at which Ω_{00}^2 changes from positive to negative occurs at progressively lower λ_i's, implying that the segment of marginal stability shortens as the size of the kernel support increases. We see that for $D \geqslant 1$, unstable behavior occurs around values of λ_i close to unity, that is, when the ADKE method essentially reduces to the fixed width kernel approach for which $h_i = h_0$. Thus, the ADKE method affects the behavior of standard SPH in the short wavelength limit, removing the instability provided that the two free parameters κ and ϵ in Eq. (14) are chosen such that λ_i falls to the left of the point where $\Omega_{00}^2 = 0$. A qualitatively similar analysis is obtained when the cubic B-spline kernel (45) is used.

5.2. Case in which $\alpha \neq 0$ and $g_1 = 0$

When artificial viscosity is allowed, the solution of the dispersion relation is given by Eq. (43). Figs. 2 and 3 display the imaginary part of the frequency as a function of λ_i for $\alpha = 1$, using the Gaussian kernel. Similar plots result for the cubic B-spline kernel. Also in this case the solution consists of two distinct complex roots, which for low values of λ_i share the same value of the imaginary part. For λ_i close to zero, the imaginary part of the frequency vanishes, indicating marginal stability. The segment for which this happens shortens as D, or equivalently, the number of nearest neighbors increases. For $D = 1$, $\mathrm{Im}(\Omega_{AV,0}) = 0$ for all values of $\lambda_i \lesssim 0.328$, whereas for $D = 4$ the same is true for $\lambda_i \lesssim 0.08$. For larger values of λ_i, the imaginary part of the frequency becomes negative, implying complete stability. At some point, the solution bifurcates into two different branches. This happens when the radicand in the first term on the right-hand side of Eq. (43) becomes negative, at which point the frequency passes from being a complex number to being a pure imaginary number.

For $D = 1$, bifurcation occurs at $\lambda_i \approx 1.232$. The point of bifurcation shifts to progressively lower values of λ_i as D is increased. In all plots, the lower branch (dashed line) keeps negative for all λ_i larger than the bifurcation value, while the upper branch of the solution (solid line) rises to higher frequencies and crosses the line where $\Omega_{AV,0} = 0$ exactly at the same value of λ_i where $\Omega_{00}^2 = 0$ in Fig. 1. Unstable behavior is therefore expected for bandwidth factors larger than this threshold value. This result clearly shows that the use of artificial viscosity does not increase the range of λ_i for which linear stability of the method is expected. Setting $\alpha \ll 1$ results in upper branches that peak at much lower positive frequencies, and therefore in slower

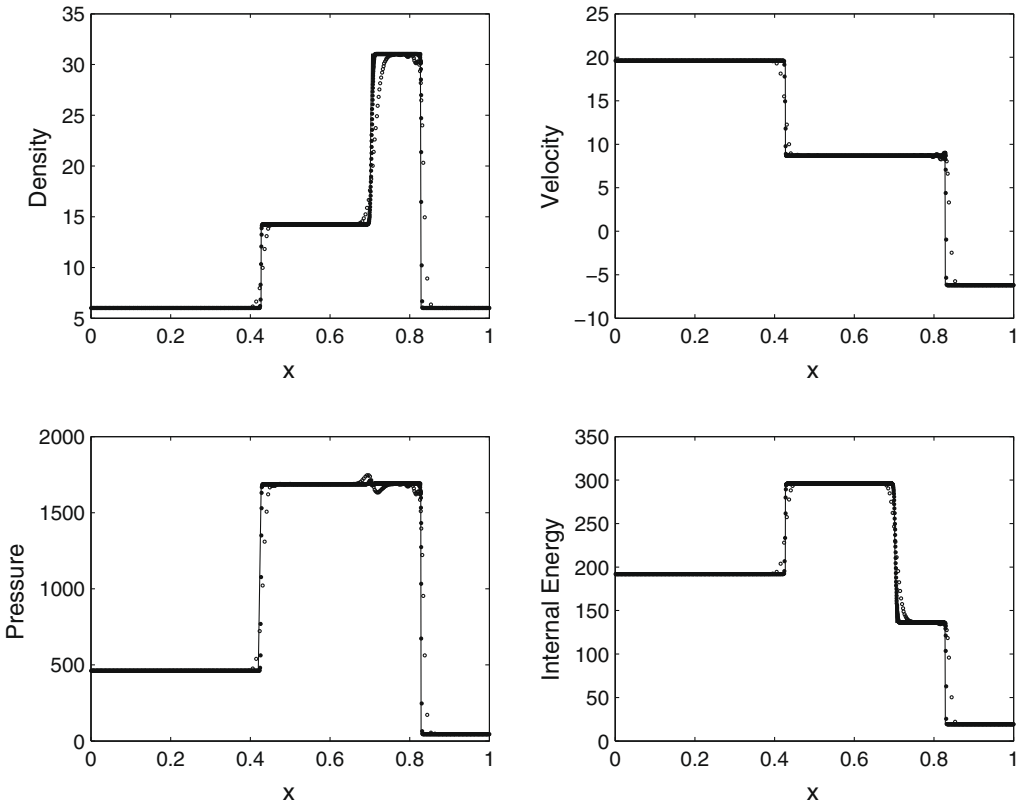

Fig. 6. Numerical results for the collision of two strong shocks as calculated using conventional SPH ($\epsilon = 0$) with 100 (open circles) and 1000 particles (filled circles). The profiles are compared with the exact solution (solid line) at $t = 0.035$ units. The calculation with 1000 particles reproduces the analytical solution with high accuracy.

growing rates of instability. As before, the range of λ_i for which stable behavior occurs decreases as the number of neighbors is increased.

5.3. Case in which $\alpha \neq 0$ and $g_1 \neq 0$

If we add an artificial heat flux, the dependence of the frequency on λ_i is given by solving the quartic polynomial of Eq. (32). This time the solution admits four independent complex roots for the frequency. Figs. 4 and 5 shows the imaginary part of these four roots as a function of λ_i for $\alpha = 1$ and $g_1 = 0.2$, using the Gaussian kernel and the same parameters as before. For low values of λ_i, the imaginary part of all four frequencies vanishes for a short interval, which becomes shorter as D is increased. As a consequence, the solution is marginally stable in these regions. At $\lambda_i \approx 0.328$, the solution bifurcates into three distinct branches for $D = 1$. The same is also true for all other values of D, with the bifurcation point shifting to lower values of λ_i for larger D (i.e., $\lambda_i \approx 0.08$ for $D = 4$). In all plots, the upper branch (dotted line) depicts the most relevant root for the purposes of our analysis. The other two frequencies (solid and dot–dashed lines) correspond to stable solutions, with $\mathrm{Im}(\Omega_{AV,AH}) < 0$. At higher λ_i's, the lowest branch (solid line) undergoes a new bifurcation (at $\lambda_i \approx 1.232$ for $D = 1$ and $\lambda_i \approx 0.312$ for $D = 4$). For $D = 1$ and $2/3$, this part of the solution is the same of that displayed in Figs. 2 and 3, with the upper branch (dashed line) rising and becoming positive at $\lambda_i \approx 1.416$ (for $D = 1$) and ≈ 0.944 (for $D = 3/2$). However, for $D \geqslant 2$ the solution changes qualitatively as the lowest initial branch (solid line) bifurcates into two new frequencies which always correspond to stable solutions, with $\mathrm{Im}(\Omega_{AV,AH}) < 0$ for most of the entire λ_i spectrum.

The appearance of the upper branch (dotted line) at low values of λ_i means that the linear stability of the method is clearly affected by the artificial heating. If lower values of g_1 are tried, the result will be qualitatively similar except that the upper branch will peak at much lower positive values of $\mathrm{Im}(\Omega_{AV,AH})$, resulting in a decreased rate of growth of the instability. Therefore, it appears that dropping the first term on the right-hand side of Eq. (11) may improve the stability properties of the method. However, we shall see in next section that for applications of the method to shock problems, the numerical solution near a contact discontinuity improves when g_1 is either < 0.01 or, in any case, much lower than g_2. It should be noticed that for finite values of g_1, the present analysis still predicts stable solutions provided that λ_i is sufficiently small. In shock simulations, this occurs for a wide range of the ADKE parameters κ and ϵ, with little dependence on the spatial resolution allowed.

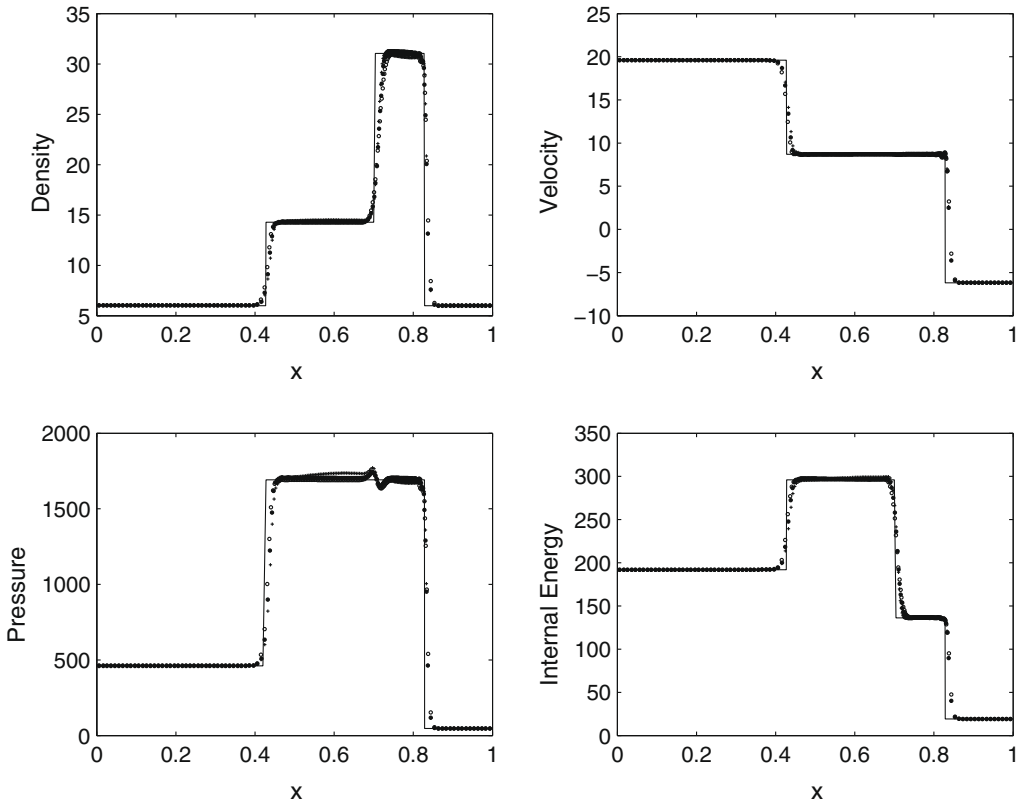

Fig. 7. Numerical results for the collision of two strong shocks as calculated using the ADKE method with 100 particles and different choices of the sensitivity parameter: $\epsilon = 0.2$ (open circles), $\epsilon = 0.5$ (filled circles), and $\epsilon = 0.8$ (crosses). The numerical solutions are compared with the exact one (solid line) at $t = 0.035$ units.

6. Convergence and consistency

In order to study the consistency of our SPH scheme (i.e., its convergence to a physical solution) we parallel the analysis performed by Rasio [53] for the propagation of a linear acoustic wave in one-space dimension. In particular, consistency of SPH will demand considering the behavior of the solution as a function of three independent parameters, namely the total number of particles N filling the computational domain, the number of neighbors $\mathcal{N}_s$, and the smoothing length h. In practice, convergence towards the exact solution requires $N \to \infty$ and $h \to 0$, whereas full consistency of SPH requires both $N \to \infty$ and $\mathcal{N}_s \to \infty$ along with $h \to 0$ such that $\mathcal{N}_s/N \to 0$ [53].

The exact dispersion relation for the propagation of a longitudinal sound wave is given by Eq. (18) and its counterpart SPH form by Eq. (37), where the indexed quantities in this latter expression are defined by the summations (20)–(26). This relation has been derived for the case of a one-dimensional gas represented by an infinite string of equidistant SPH particles, all with the same mass. This simple problem allows us to calculate analytically the error present in the SPH solution and to study its behavior in terms of $N, \mathcal{N}_s$, and h. In Section 4.2, we have also shown that in the long wavelength limit, which corresponds to $k \to 0$, Eq. (37) becomes identical to the continuum dispersion relation (18) as long as $h/\Delta x_0 \to \infty$. This latter limit is equivalent to a large number of neighbors, $\mathcal{N}_s \to \infty$. Now suppose that we take the $k \to 0$ and $N \to \infty$ limits of Eq. (37) by keeping the value of the ratio $h/\Delta x_0$ arbitrary, so that $\mathcal{N}_s$ remains finite. In this case, Eq. (37) takes the form

$$\frac{c_{\rm SPH}^2}{c_0^2} = \frac{(\gamma-2)}{\gamma}\left(\Delta x_0 \sum_{j=1}^{\mathcal{N}_s} x_{0,ij}\frac{\partial W_{ij}}{\partial x_{0,i}}\right)^2 + \frac{1}{\gamma}\Delta x_0 \sum_{j=1}^{\mathcal{N}_s} x_{0,ij}^2 \frac{\partial^2 W_{ij}}{\partial x_{0,i}^2}, \tag{46}$$

where we have made use of Eq. (31) and defined $c_{\rm SPH}^2 = \omega^2/k^2$. It is easy to see from Eq. (46) that if we shift the position of particle i to the origin so that $x_{0,i} = 0$, the first term on the right-hand side vanishes and so only the second term contributes. Using the kernels defined by Eqs. (44) and (45) to evaluate Eq. (46), we may see that $c_{\rm SPH}$ does not converge to c_0. This implies that taking the combined limits $N \to \infty$ and $h \to 0$ while keeping $\mathcal{N}_s$ constant results in an inconsistent scheme. In order to recover consistency both N and $\mathcal{N}_s$ should be increased, with N increasing faster than $\mathcal{N}_s$ so that $h \to 0$ in the process [53]. This is precisely what we did in Section 4.2. However, to correctly determine the leading error term in the dispersion relation we must follow a slightly different approach. First, we take the limit when $\mathcal{N}_s \gg 1$ so that the summations in Eq. (37) can be replaced by integrals over the infinite string of particles. In doing so, we find that

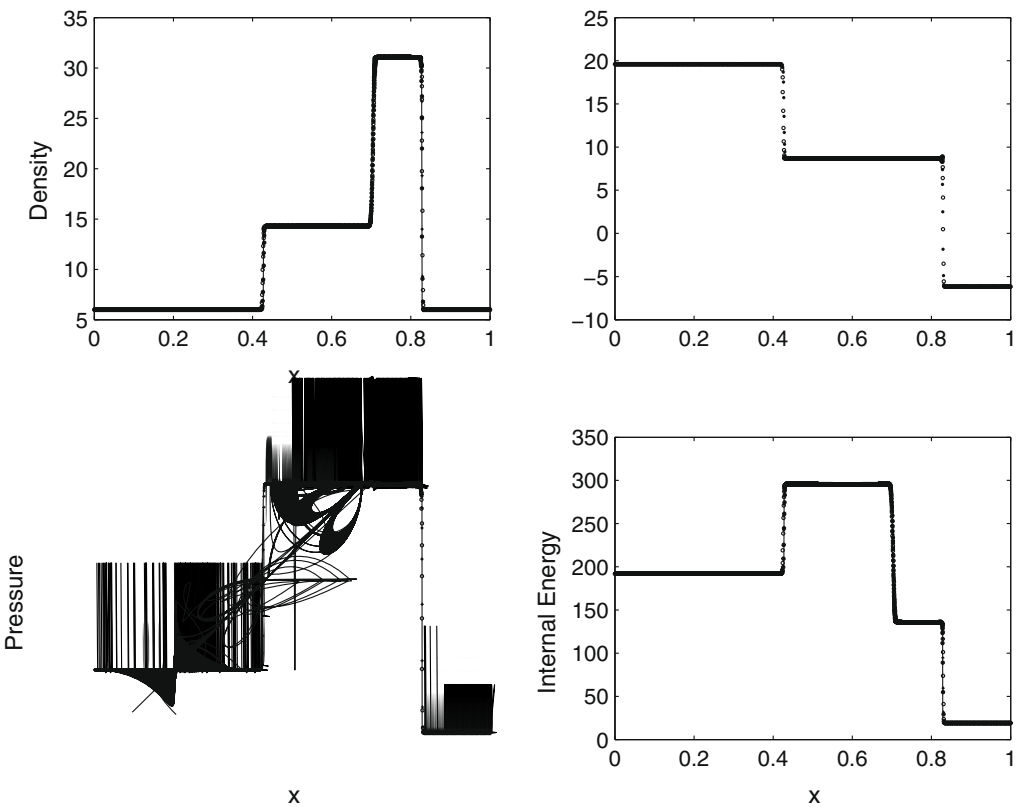

Fig. 8. Numerical results for the collision of two strong shocks as calculated using the ADKE method with 1000 particles and different choices of the sensitivity parameter: $\epsilon = 0.2$ (open circles), $\epsilon = 0.5$ (filled circles), and $\epsilon = 0.8$ (crosses). The numerical solutions are compared with the exact one (solid line) at $t = 0.035$ units.

$$\frac{c_{\mathrm{SPH}}^2}{c_0^2} \to \frac{(\gamma-2)}{\gamma}\left[\left(\int_{-\infty}^{+\infty}\cos(kx)W(x,h)dx\right)^2-\left(\int_{-\infty}^{+\infty}\sin(kx)W(x,h)dx\right)^2\right]+\frac{2}{\gamma}\int_{-\infty}^{+\infty}\cos(kx)W(x,h)dx, \tag{47}$$

which is valid for any value of the wavenumber k. Next, we calculate the limiting form of Eq. (47) when $k \to 0$, which yields

$$\frac{c_{\mathrm{SPH}}^2}{c_0^2} \to 1-\left(1-\frac{1}{\gamma}\right)k^2\int_{-\infty}^{+\infty}x^2W(x,h)dx+\mathcal{O}(k^4), \tag{48}$$

where we have used Taylor expansions for the sine and cosine functions. This expression shows that the leading error term in the SPH dispersion relation is $\mathcal{O}(k^2)$ and that the SPH solution converges to the exact solution in the limits $\mathcal{N}_s/N \to 0$ and $h \to 0$. We may also see from Eq. (48) that for isothermal gases ($\gamma = 1$) the integral on the right-hand side vanishes, producing a leading error of $\mathcal{O}(k^4)$. We note that consistency of SPH is, in general, independent of the form of the smoothing kernel. However, noting that for a string of SPH particles $\mathcal{N}_s = 2D$ and that $W(x,h) \sim w(x)/h$, where $w(x)$ is the dimensionless form of the kernel and $h = D\Delta x_0\lambda$ for the ADKE procedure, we see that improved accuracy of the scheme can be obtained for larger values of the dilation factor, D, provided that stable values of λ are chosen. In next section we shall see that, for practical purposes, accurate solutions with the ADKE scheme are always obtained when $\mathcal{N}_s/N = 2D/N \ll 1$ with little dependence on the smoothness of the kernel.

7. Numerical tests

The ADKE method has been shown to work quite well for a number of one- and two-dimensional shock test problems [36], involving the Sod's [37] shock-tube, the blast wave [33], the wall shock, the cylindrical Noh's [44] shock implosion, and the Sedov [54] point explosion. In this section, we test the ability of the method for a suite of more stringent test cases. Because of the short wavelength character of the instability, we expect the outcome of the numerical simulations to fit fairly

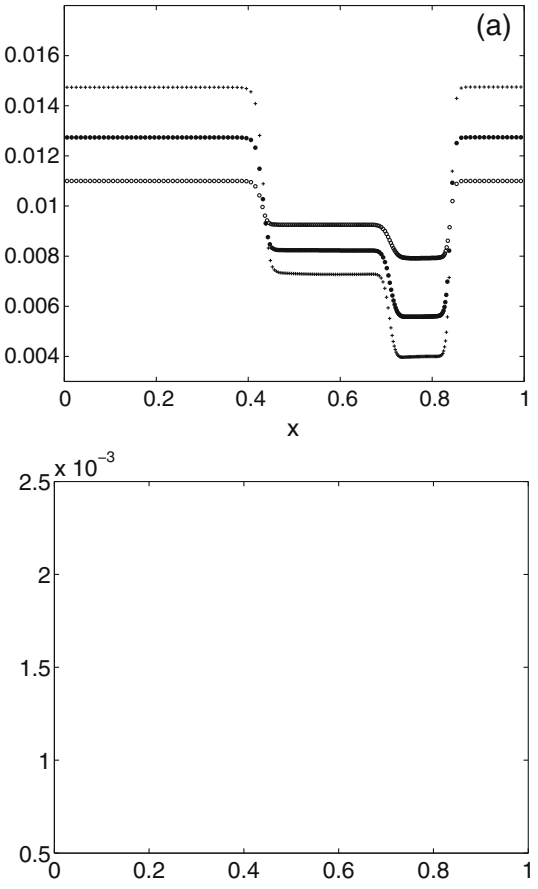

well the predictions of the linear analysis. We anticipate that the numerical solutions are essentially independent of whether Eqs. (44) or (45) is used.

7.1. Collision of two strong shocks

As a first test we consider the collision of two strong shocks introduced by Toro [38]. The initial conditions consist of gas with $\gamma = 1.4$ and left ($x < 0.4$) and right states ($x \geqslant 0.4$) given by $\rho_L = 5.99924, v_L = 19.5975, p_L = 460.894$ and $\rho_R = 5.99242, v_R = -6.19633, p_R = 46.0950$, respectively. The solution to this problem contains a left facing shock, moving slowly to the left, a right traveling contact discontinuity, and a shock wave moving to the right. This test model has been recently recalculated by Ferrari et al. [32] to test their Godunov-type SPH scheme in Lagrangian coordinates. Transmissive boundary conditions are applied at the extremes $x = 0$ and $x = 1$ of the computational domain.

We consider two independent sequences of calculations for varied sizes of the kernel support ($0 \leqslant D \leqslant 4$) and values of the ADKE sensitivity parameter ($0 \leqslant \epsilon \leqslant 0.8$), which differ only in the spatial resolution allowed. One sequence uses 100 particles and the other 1000 particles, all uniformly distributed along the interval $0 \leqslant x \leqslant 1$. In all cases, we use $\alpha = \beta = 1$, $g_1 = 0.02, g_2 = 0.4, \kappa = 1$, and a constant time step ($\Delta t = 5 \times 10^{-5}$ for the runs with 100 particles and 5×10^{-6} for the runs with 1000 particles). Fig. 6 shows the numerical profiles for a calculation with 100 (open circles) and 1000 particles (filled circles) as compared with the exact solution (solid line) at $t = 0.035$ units, using standard SPH (i.e., $\epsilon = 0$) and $D = 3/2$. We see that the low-resolution run (open circles) produces too smooth density and internal energy profiles at the contact discontinuity, causing a large amplitude wiggling in the pressure. Also the left and right shocks are not well solved and small amplitude oscillations are present for the density, velocity, and pressure in the star region of the flow close to the right shock. When the resolution is increased to 1000 particles (filled circles), standard SPH produces much sharper profiles for this test. The contact discontinuity is now very well solved and only a small-amplitude wiggle is still present in the pressure. The left and right shocks are also well reproduced, with postshock values within a few percent of the exact solution. Our results show that standard SPH yields accurate profiles for this test provided that the spatial resolution is increased.

With the ADKE method the solution does not improve much when working at low resolution. This is shown in Fig. 7, where the numerical solution with $D = 1$ is compared for three different choices of ϵ, namely $\epsilon = 0.2$ (open circles), 0.5 (filled circles), and 0.8 (crosses). The solutions are similar to the one in Fig. 6 with $\epsilon = 0$ and, except for the large amplitude wiggling

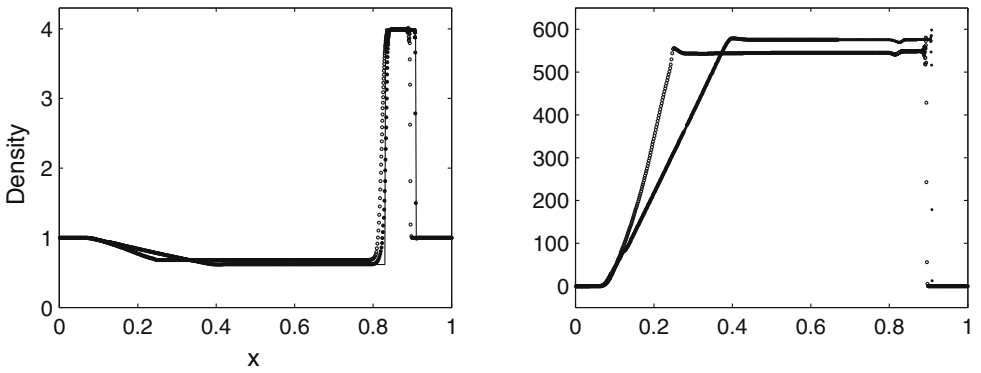

in the pressure, to those obtained by Ferrari et al. [32], using their Godunov-type SPH method with 100 particles. When the same models are rerun with 1000 particles, the results improve again as shown in Fig. 8 for $D = 3/2$. Only very small differences appear when ϵ is varied. For these runs, the variation of $\lambda_i = h_i/h_0$ with distance is depicted in Fig. 9. We see that λ_i varies in a small interval that falls well within the region where the linear analysis predicts marginal stability (see Figs. 4 and 5). The largest variations of λ_i always occur for $\epsilon = 0.8$ (crosses), where the bandwidth factors are more sensitive to variations in the density. Increased values of the dilation factor result essentially in the same profiles of Fig. 8.

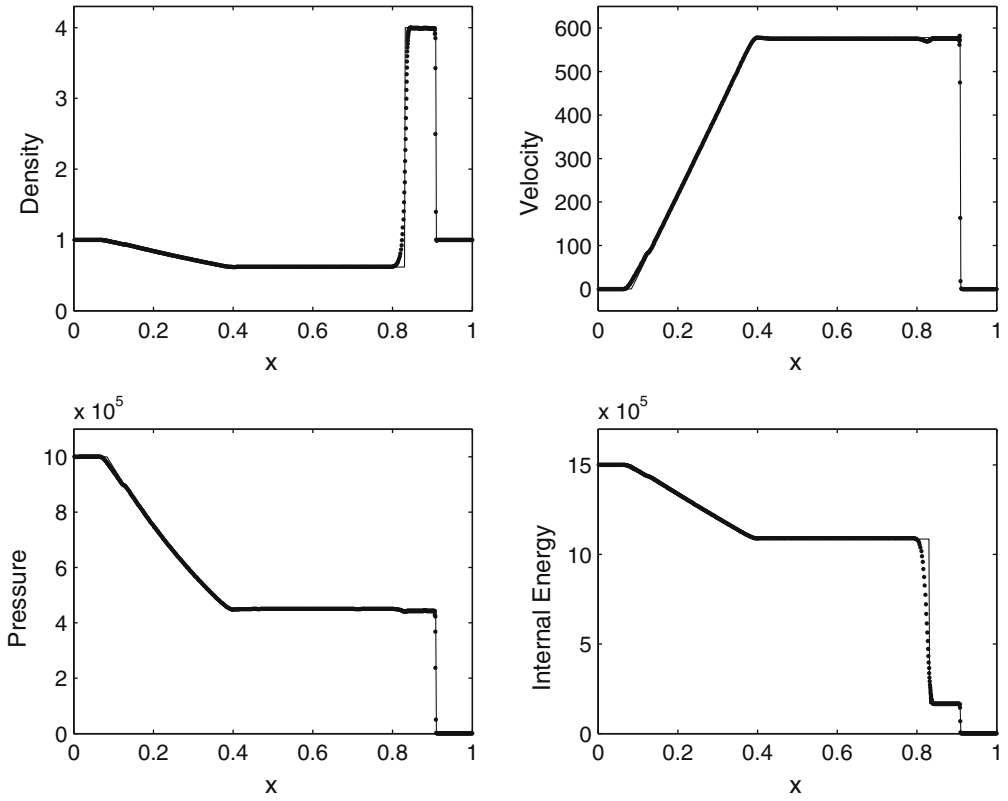

Fig. 11. Numerical results of the shock-tube problem containing a very strong shock as calculated with 1000 particles, using the ADKE method (filled circles) with a larger size of the kernel support ($D = 3/2$), $\epsilon = 0.8$, $g_1 = 0.2$, and $g_2 = 1$.

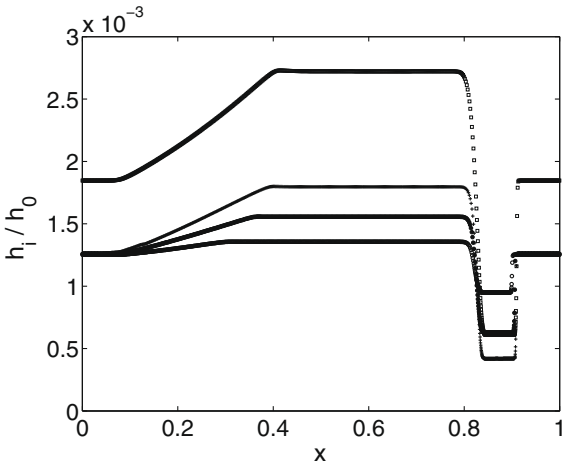

Fig. 12. Spatial dependence of the bandwidth factors, $\lambda_i = h_i/h_0$, for four separate runs of the strong shock-tube with $D = 1$ and different choices of the sensitivity parameter: $\epsilon = 0.2$ (open circles), $\epsilon = 0.5$ (filled circles), and $\epsilon = 0.8$ (crosses). For comparison, the spatial dependence of λ_i is also shown for the run of Fig. 11 (open squares).

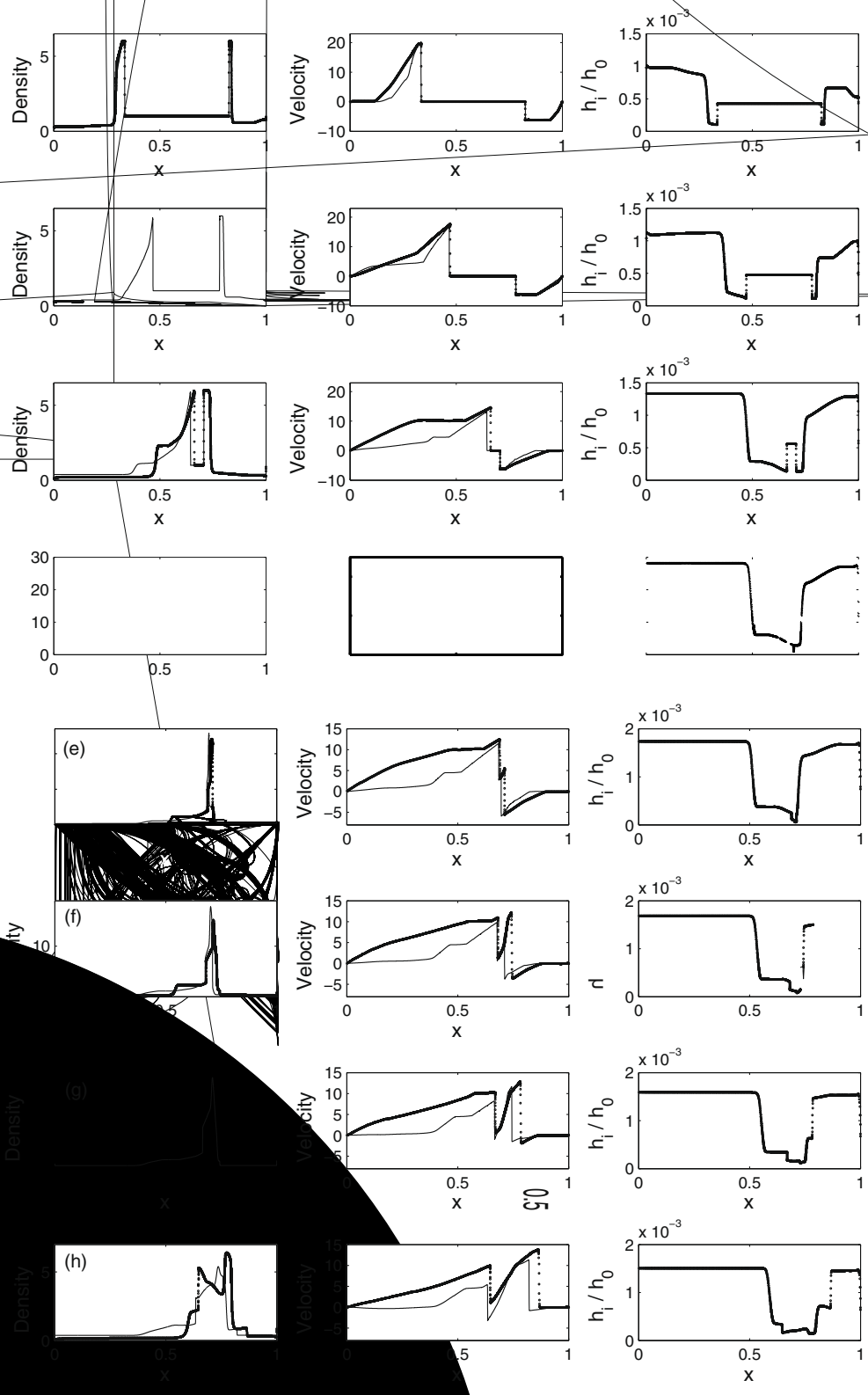

y, and bandwidth factor profiles for the two blast waves test as calculated with 5000 particles, using standard SPH ($\epsilon = 0$, solid line) filled dots) with $D = 1$, $\epsilon = 0.8$, $g_1 = 0.2$, and $g_2 = 1$. The sequence of times is: (a) 0.010, (b) 0.016, (c) 0.026, (d) 0.028, (e) 0.030, (f) 0.038 units. While standard SPH performs bad for this test, the ADKE scheme reproduces all features of the multiple wave res quite well with the accurate solution reported in [33].

7.2. Shock-tube containing a very strong shock

A more difficult test calculation has been proposed by Fryxell et al. [39]. This test is a modified shock-tube problem containing a very strong shock and involving extremely supersonic flows. The initial conditions consist of an ideal gas at rest with $\gamma = 5/3$ and left ($x < 0.6$) and right ($x \geqslant 0.6$) states given by $\rho_L = 1, p_L = 10^6, v_L = 0$ and $\rho_R = 1, p_R = 1, v_R = 0$. The initial pressure on the left-hand side is 10^6 times that of the right-hand side, resulting in a Mach 771 shock. An accurate description of this test problem requires an initial high-spatial resolution even when working with high-quality Godunov-type schemes. For this test model we have also carried out a series of calculations all with 1000 equidistant particles inside the interval $0 \leqslant x \leqslant 1$ and varying values of D, ϵ, g_1, and g_2. A constant timestep ($\Delta t = 5 \times 10^{-6}$) with $\kappa = 1$ and $\alpha = \beta = 1$ have been used for all runs.

Fig. 10 compares the numerical solutions as obtained using standard SPH ($\epsilon = 0$, open circles) and the ADKE method with $\epsilon = 0.8, g_1 = 0.2$, and $g_2 = 0.4$ (filled circles) with the exact solution (solid line) at $t = 4 \times 10^{-4}$ units. For both runs we have set $D = 1$. The standard SPH fails to accurately reproduce this test, giving a bad description of the rarefaction wave and wrong postshock values of the pressure, velocity, and internal energy. Conversely, the ADKE method produces a much more accurate solution except for the small roundings in the density and internal energy at the top and foot of the contact discontinuity, which are in turn responsible for the small wiggles in the pressure and velocity. We also note the presence of an upward spike in the velocity at the position of the shock. In particular, the intensity of this unphysical spike can be strongly reduced by rising the value of g_2, as shown in Fig. 11 for a similar calculation with $D = 3/2$ and $g_2 = 1$. In the same way, the small roundings at the top and foot of the contact discontinuity can be slightly sharpened by reducing the value of g_1. Finally, Fig. 12 shows the variation of λ_i with position for a sequence of calculations with $D = 1$ and $\epsilon = 0.2$ (open circles), 0.5 (filled circles), and 0.8 (crosses). For comparison, the λ_i profile for the calculation of Fig. 11 with $D = 3/2$ (open squares) is also shown. In all cases, the values of λ_i always fall within the range where marginal stability is predicted according to Figs. 4 and 5.

7.3. Two interacting blast waves

We now test the response of the method against an extremely difficult problem involving multiple interactions of strong shocks and rarefactions with each other and with contact discontinuities. This test is fully described by Woodward and Colella [33] and was originally introduced to illustrate the strong relationship between the accuracy of the overall flow and the

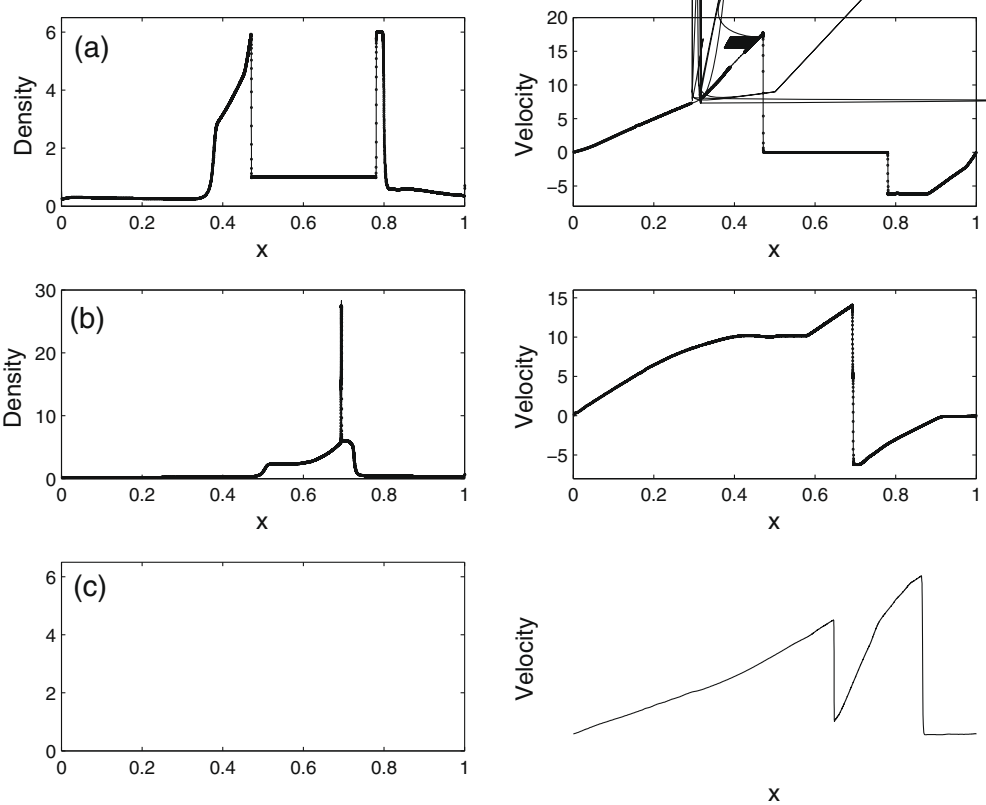

Fig. 14. Same ADKE calculation as in Fig. 13 but with $D = 2$ (filled circles) at (a) $t = 0.016$, (b) 0.028, and (c) 0.038 units. The solid line corresponds to the accurate ADKE solution of Fig. 13.

thinness of the discontinuities on the grid for Godunov-type methods. The initial conditions consist of an ideal gas at rest with $\gamma = 1.4$ and three constant states given by $(\rho_L = 1, v_L = 0, p_L = 10^3)$ for $0 \leqslant x < 0.1$, $(\rho_M = 1, v_M = 0, p_M = 10^{-2})$ for $0.1 \leqslant x < 0.9$, and $(\rho_R = 1, v_R = 0, p_R = 10^2)$ for $0.9 \leqslant x < 1$. The boundaries at $x = 0$ and $x = 1$ are solid walls. Therefore, we apply reflective boundary conditions for the velocity and continuity conditions for all other variables at the walls. These conditions result in two blast waves that collide, producing a new contact discontinuity. The evolution for this test is quite complex and we refer the reader to [33] for a detailed discussion of the various interactions that occur.

Since there is no known analytical solution available for this problem, we have developed an accurate solution using the ADKE method with 5000 equidistant particles inside the interval $0 \leqslant x \leqslant 1$. The best solution was chosen from a series of runs with varied values of D, ϵ, and g_2. The other parameters were fixed to $\kappa = 1$, $g_1 = 0.2$, and $\alpha = \beta = 1$. The best solution was obtained for $D = 1$, $\epsilon = 0.8$, and $g_2 = 1$ and is displayed in Fig. 13 (open circles) at the same discrete times of Fig. 2 in [33], where an accurate solution to this problem is given. A close comparison between both solutions shows that the ADKE scheme has been quite successful at reproducing the several complex details with high accuracy. The solid line in Fig. 13 also depicts the profiles as they were obtained using standard SPH ($\epsilon = 0$). The two blast waves penetrate into the intermediate low pressure gas. Meantime, strong rarefaction waves form and propagate outward towards the walls, where they are reflected back. The Mach numbers of the left and right shocks are approximately 170 and 51, respectively. This difference causes the two shocks to exhibit structural differences, as seen in Fig. 13(a)–(c). At $t = 0.028$ (Fig. 13(d)), the shocks collide and produce a sharp density spike. The reflected rarefaction waves have by this time caught up with the shocks and weakened them. On either side of the density spike, there is a contact discontinuity. The profiles of the density and velocity shown in Fig. 13(e)–(h) are the result of multiple interactions of strong nonlinear continuous waves and a variety of discontinuities.

The effects of increasing the dilation factor to $D = 2$ are shown in Fig. 14 (open circles) at $t = 0.016, 0.028,$ and 0.038 units. The solution is compared with that of Fig. 13, which is now represented by the solid line. We see that both solutions are almost identical except that the sharp density spike, which forms when the two blast waves collide, appears to be slightly down for the case when $D = 2$. This is an affect of broadening the kernel which increases the amount of smoothing. In addition, Figs. 15 and 16 show the solution at the same times of Fig. 14, when the resolution has been decreased to 2500 and 1000 particles, respectively. We see that dropping the resolution to 2500 particles does not appear to affect the evolution, apart from a further slight reduction of the density spike. When 1000 particles are used, the evolution results in a much short density spike at the time when the two blast waves collide and in a smoother profile in the higher density regions at $t = 0.038$, resulting from the interaction of the left-moving rarefaction wave with the central contact discontinuity. These results give

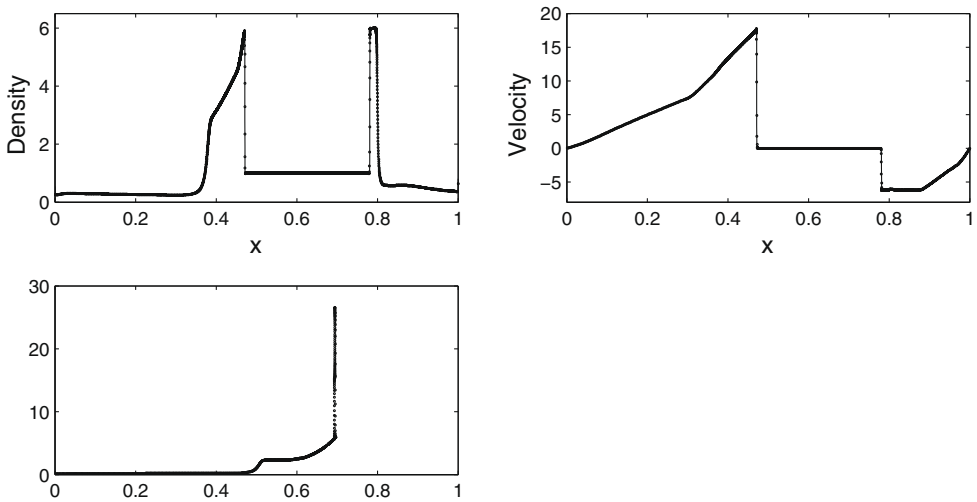

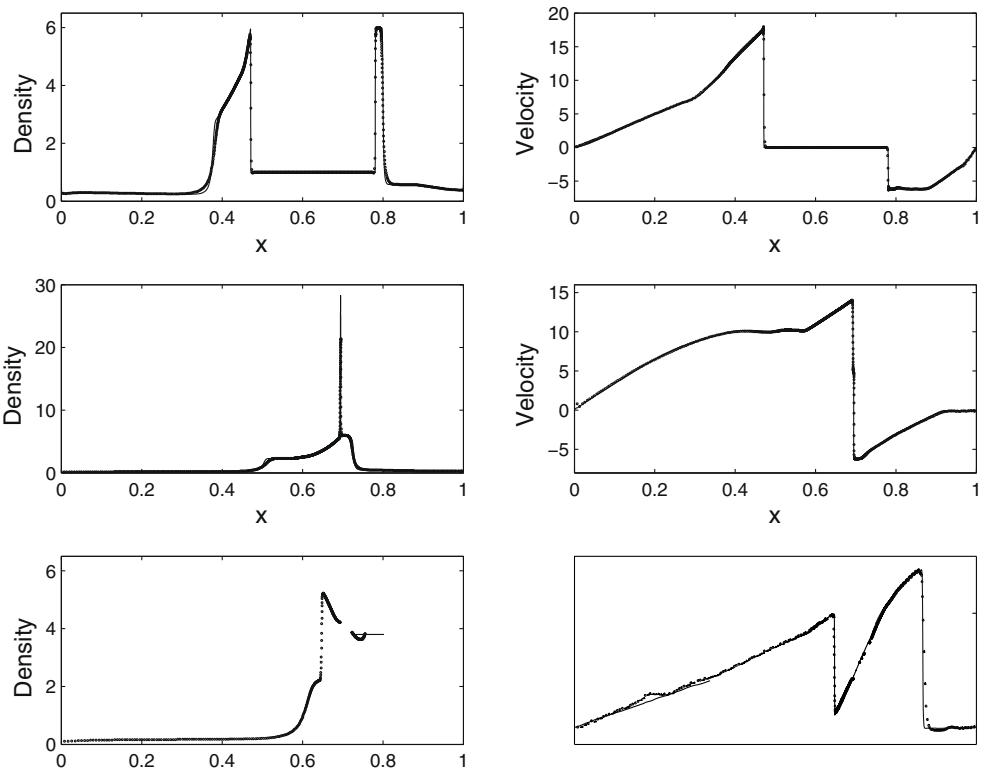

Fig. 16. Same ADKE calculation as in Fig. 13 but with 1000 particles (filled circles) at (a) $t = 0.016$, (b) 0.028, and (c) 0.038 units. The solid line corresponds to the accurate ADKE solution of Fig. 13.

a convincing evidence of the stability and resolving power of the SPH method when it is combined with the ADKE procedure.

8. Conclusions

We have described an alternative SPH scheme to SPH Godunov-type methods for the simulation of highly supersonic compressible flows involving strong shock waves. The method combines standard SPH with an *adaptive density estimation kernel* (ADKE) algorithm, which solves the flow in low-density regions with the minimum necessary smoothing. In brief, the ADKE method consists of constructing a collection of local bandwidth factors, or kernel estimates, using the particle density distribution. Unlike existing adaptive SPH formulations, this procedure needs less broad kernels in regions where the density is low. The definition of the local bandwidth factors involves two free parameters, which depending on the problem at hand, can be conveniently chosen to reduce the rates of numerical dissipation and diffusion.

We have performed a von Neumann stability analysis of the SPH equations for an ideal gas to study the stability of the method in response to propagating longitudinal sound waves. Solution of the dispersion relation in the short wavelength limit shows that the method is stable for a wide range of the ADKE parameters provided that the linear contribution of the artificial heat flux is always kept at a sufficiently low value. This is usually the case near a strong shock, where the nonlinear contribution of the artificial heat flux overwhelms the linear one. Application of the method to high Mach number shocks confirms the predictions of the linear stability analysis. We have carried out a large number of simulations with varied initial number of particles and values of the ADKE parameters for a set of difficult test problems, involving the collision of two strong shock waves [38], the shock-tube with a very strong shock [39], and the two interacting blast waves [33]. These tests complement the suite of one- and two-dimensional tests that have been previously carried out with the present method by Sigalotti et al. [36]. The results obtained for this new set of tests demonstrate that the method performs quite well at handling complex phenomena involving multiple interactions of strong shocks and rarefaction waves with each other and with contact discontinuities. The accuracy of the results is comparable to that obtained with Godunov-type schemes and SPH formulations based on Riemann solvers. The ADKE scheme has other advantages in that it is quite simple to implement and does not require special modifications when applied to two- and three-dimensional flows.

References

[1] L.B. Lucy, A numerical approach to the testing of the fission hypothesis, Astron. J. 83 (1977) 1013.
[2] R.A. Gingold, J.J. Monaghan, Smoothed particle hydrodynamics: Theory and application to non-spherical stars, Mon. Not. Royal Astron. Soc. 181 (1977) 375.
[3] R.A. Gingold, J.J. Monaghan, The collapse of a rotating non-axisymmetric isothermal cloud, Mon. Not. Royal Astron. Soc. 197 (1981) 461.
[4] G. Phillips, J.J. Monaghan, A numerical method for three-dimensional simulations of collapsing, isothermal, magnetic clouds, Mon. Not. Royal Astron. Soc. 216 (1985) 883.
[5] A.E. Evrard, Beyond N-body – 3D cosmological gas dynamics, Mon. Not. Royal Astron. Soc. 235 (1988) 911.
[6] J.J. Monaghan, J.C. Lattanzio, A simulation of the collapse and fragmentation of cooling molecular clouds, Astrophys. J. 375 (1991) 177.
[7] R.P. Nelson, J.C.B. Papaloizou, Three-dimensional hydrodynamic simulations of collapsing prolate clouds, Mon. Not. Royal Astron. Soc. 265 (1993) 905.
[8] P.R. Shapiro, H. Martel, J.V. Villumsen, J.M. Owen, Adaptive smoothed particle hydrodynamics with applications to cosmology: Methodology, Astrophys. J. Suppl. Ser. 103 (1996) 269.
[9] M.R. Bate, Collapse of a molecular cloud core to stellar densities: The first three-dimensional calculations, Astrophys. J. 508 (1998) L95.
[10] R.S. Klessen, A. Burkert, M.R. Bate, Fragmentation of molecular clouds: The initial phase of a stellar cluster, Astrophys. J. 501 (1998) L205.
[11] V. Springel, The cosmological simulation code GADGET-2, Mon. Not. Royal Astron. Soc. 364 (2005) 1105.
[12] G. Arreaga-García, J. Klapp, L.Di G. Sigalotti, R. Gabbasov, Gravitational collapse and fragmentation of molecular cloud cores with GADGET-2, Astrophys. J. 666 (2007) 290.
[13] H. Takeda, S.M. Miyama, M. Sekiya, Numerical simulation of viscous flow with smoothed particle hydrodynamics, Prog. Theor. Phys. 92 (5) (1994) 939.
[14] J.J. Monaghan, Simulating free surface flows with SPH, J. Comput. Phys. 110 (1994) 399.
[15] J.J. Monaghan, A. Kocharyan, SPH simulation of multi-phase flow, Comput. Phys. Commun. 87 (1995) 225.
[16] O. Kum, W.G. Hoover, H.A. Posch, Viscous conducting flows with smooth-particle applied mechanics, Phys. Rev. E 52 (5) (1995) 4899.
[17] J.P. Morris, P.J. Fox, Y. Zhu, Modeling low Reynolds number incompressible flows using SPH, J. Comput. Phys. 136 (1997) 214.
[18] S. Nugent, H.A. Posch, Liquid drops and surface tension with smoothed particle applied mechanics, Phys. Rev. E 62 (4) (2000) 4968.
[19] A. Colagrossi, M. Landrini, Numerical simulation of interfacial flows by smoothed particle hydrodynamics, J. Comput. Phys. 191 (2003) 448.
[20] L.Di G. Sigalotti, J. Klapp, E. Sira, Y. Meleán, A. Hasmy, SPH simulations of time-dependent Poiseuille flow at low Reynolds numbers, J. Comput. Phys. 191 (2003) 622.
[21] H. López, L.Di G. Sigalotti, Oscillation of viscous drops with smoothed particle hydrodynamics, Phys. Rev. E 73 (2006). 051201-1.
[22] L.D. Libersky, A.G. Petschek, T.C. Carney, J.R. Hipp, F.A. Allahdadi, High strain Lagrangian hydrodynamics. A three-dimensional SPH code for dynamic material response, J. Comput. Phys. 109 (1993) 67.
[23] P.W. Randles, T.C. Carney, L.D. Libersky, J.D. Renick, A.G. Petschek, Calculation of oblique impact and fracture of tungsten cubes using smoothed particle hydrodynamics, Int. J. Impact Eng. 17 (1995) 661.
[24] D.A. Mandell, C.A. Wingate, L.A. Schwalbe, Computational brittle fracture using smooth particle hydrodynamics, in: 14th US Army Symposium on Solid Mechanics, Myrtle Beach, South Carolina, 16–18 October, 1996.
[25] J.K. Chen, F.A. Allahdadi, T.C. Carney, High-velocity impact of graphite/epoxy composite laminates, Comput. Sci. Tech. 57 (1997) 1369.
[26] J.J. Monaghan, SPH without a tensile instability, J. Comput. Phys. 159 (2000) 290.
[27] J.P. Gray, J.J. Monaghan, R.P. Swift, SPH elastic dynamics, Comput. Meth. Appl. Mech. Eng. 190 (2001) 6641.
[28] R.E. Attwood, S.P. Goodwin, A.P. Whitworth, Adaptive smoothing lengths in SPH, Astron. Astrophys. 464 (2007) 447.
[29] J.J. Monaghan, SPH and Riemann solvers, J. Comput. Phys. 136 (1997) 298.
[30] S. Inutsuka, Reformulation of smoothed particle hydrodynamics with Riemann solver, J. Comput. Phys. 179 (2002) 238.
[31] S.-H. Cha, A.P. Whitworth, Implementation and tests of Godunov-type particle hydrodynamics, Mon. Not. Royal Astron. Soc. 340 (2003) 75.
[32] A. Ferrari, M. Dumbser, E.F. Toro, A. Armanini, A new stable and consistent version of the SPH method in Lagrangian coordinates, SPHERIC – Smoothed Particle Hydrodynamics European Research Interest Community, 2nd International Workshop, Universidad Poltécnica de Madrid, Madrid, 23–18 May, 2007.
[33] P. Woodward, P. Colella, The numerical simulation of two-dimensional fluid flow with strong shocks, J. Comput. Phys. 54 (1984) 115.
[34] S. Børve, M. Omang, J. Trulsen, Regularized smoothed particle hydrodynamics: A new approach to simulating magnetohydrodynamics shocks, Astrophys. J. 561 (2001) 82.
[35] B.W. Silverman, Density Estimation for Statistics and Data Analysis, Chapman & Hall, London, 1996.
[36] L.Di G. Sigalotti, H. López, A. Donoso, E. Sira, J. Klapp, A shock-capturing SPH scheme based on adaptive kernel estimation, J. Comput. Phys. 212 (2006) 124.
[37] G.A. Sod, A survey of several finite difference methods for systems of nonlinear hyperbolic conservation laws, J. Comput. Phys. 27 (1978) 1.
[38] E.F. Toro, Riemann Solvers and Numerical Methods for Fluid Dynamics: A Practical Introduction, Springer, Berlin, 1999.
[39] B.A. Fryxell, P.R. Woodward, P. Colella, K.-H. Winkler, An implicit–explicit hybrid method for Lagrangian hydrodynamics, J. Comput. Phys. 63 (1986) 283.
[40] J. Bonet, T.-S.L. Lok, Variational and momentum preservation aspects of smoothed particle hydrodynamics formulations, Comput. Meth. Appl. Mech. Eng. 180 (1999) 97.
[41] J.J. Monaghan, R.A. Gingold, Shock simulation by the particle method SPH, J. Comput. Phys. 52 (1983) 374.
[42] J.C. Lattanzio, J.J. Monaghan, H. Pongracic, M.P. Schwarz, Controlling penetration, SIAM J. Sci. Stat. Comput. 7 (1986) 591.
[43] J.J. Monaghan, An introduction to SPH, Comput. Phys. Commun. 48 (1988) 89.
[44] W.F. Noh, Errors for calculations of strong shocks using an artificial viscosity and an artificial heat flux, J. Comput. Phys. 72 (1978) 78.
[45] L.Di G. Sigalotti, H. López, Adaptive kernel estimation and the SPH tensile instability, Comput. Math. Appl. 55 (2008) 23.
[46] L. Hernquist, N. Katz, TREESPH – A unification of SPH with the hierarchical tree method, Astrophys. J. Suppl. Ser. 70 (1989) 419.
[47] J.W. Swegle, D.L. Hicks, S.W. Attaway, Smoothed particle hydrodynamics stability analysis, J. Comput. Phys. 116 (1995) 123.
[48] M. Schüssler, D. Schmitt, Comments on smoothed particle hydrodynamics, Astron. Astrophys. 97 (1981) 373.
[49] J.P. Morris, Analysis of Smoothed Particle Hydrodynamics with Applications, Ph.D. Thesis, Monash University, Melbourne, Australia, 1996.
[50] J.P. Morris, A study of the stability properties of smooth particle hydrodynamics, Publ. Astron. Soc. Aust. 13 (1996) 97.
[51] S. Børve, M. Omang, J. Trulsen, Two-dimensional MHD smoothed particle hydrodynamics stability analysis, Astrophys. J. Suppl. Ser. 153 (2004) 447.
[52] J.J. Monaghan, J.C. Lattanzio, A refined particle method for astrophysical problems, Astron. Astrophys. 149 (1985) 135.
[53] F.A. Rasio, Particle methods in astrophysical fluid dynamics, Prog. Theor. Phys. Suppl. 138 (2000) 609.
[54] L.I. Sedov, Similarity and Dimensional Methods in Mechanics, Academic Press Inc., New York, 1959.